

Magnetic Polaron States in Photoluminescent Carbon Dots Enable Hydrogen Peroxide Photoproduction

Lukáš Zdražil, Zdeněk Baďura, Michal Langer, Sergii Kalytchuk, David Panáček, Magdalena Scheibe, Štěpán Kment, Hana Kmentová, Muhammed Arshad Thottappali, Elmira Mohammadi, Miroslav Medved,^{*} Aristides Bakandritsos, Giorgio Zoppellaro,^{*} Radek Zbořil,^{*} and Michal Otyepka^{*}

Photoactivation of aspartic acid-based carbon dots (Asp-CDs) induces the generation of spin-separated species, including electron/hole (e^-/h^+) polarons and spin-coupled triplet states, as uniquely confirmed by the light-induced electron paramagnetic resonance spectroscopy. The relative population of the e^-/h^+ pairs and triplet species depends on the solvent polarity, featuring a substantial stabilization of the triplet state in a non-polar environment (benzene). The electronic properties of the photoexcited Asp-CDs emerge from their spatial organization being interpreted as multi-layer assemblies containing a hydrophobic carbonaceous core and a hydrophilic oxygen and nitrogen functionalized surface. The system properties are dissected theoretically by density functional theory in combination with molecular dynamics simulations on quasi-spherical assemblies of size-variant flakelike model systems, revealing the importance of size dependence and interlayer effects. The formation of the spin-separated states in Asp-CDs enables the photoproduction of hydrogen peroxide (H_2O_2) from water and water/2-propanol mixture via a water oxidation reaction.

1. Introduction


To meet the future energy demand for a carbon-neutral and fossil-fuel-unplugged civilization, effective integration of renewable power plants into the electrical grid is a prerequisite. However, due to the intermittent nature of renewable power generation (i.e., solar and wind energy), effective and practical energy storage solutions are needed to mitigate this critical

limitation of renewables. On this basis, solar energy harvested during appropriate weather conditions can be converted via artificial photosynthesis into a stable, readily accessible, and portable chemical form of high-energy-content molecules.^[1–3]

In the past, several metal-free multi-component photocatalysts have been developed for solar fuel production, being capable of fast charge transfer and efficient electron and hole separation between the individual components.^[4–6] However, it is very challenging to understand the complex nature of photoexcitation, photogenerated charge transfer, and recombination processes occurring in this multi-component photocatalytic systems, which still hinders the further development of suitable nanomaterials for artificial photosynthesis.^[7–9]

Carbon dots (CDs) are photoluminescent (PL) organic-based nanomaterials^[10–13] (size <10 nm) that exhibit great potential in advanced applications such as nanosensors,^[14–19] cellular bioimaging,^[20–23] optoelectronics,^[24–30] and as photosensitizers in solar energy conversion.^[31–37] The majority of known CDs reported in the literature are characterized by a graphitic-like core organized into intricate sp^2/sp^3 carbon networks and a surrounding shell, which, depending on the type of organic precursor used during the CDs synthetic assembly, may also

L. Zdražil, Z. Baďura, M. Langer, S. Kalytchuk, D. Panáček, M. Scheibe, Š. Kment, H. Kmentová, E. Mohammadi, M. Medved, A. Bakandritsos, G. Zoppellaro, R. Zbořil, M. Otyepka
Regional Centre of Advanced Technologies and Materials
Czech Advanced Technology and Research Institute
Palacký University Olomouc
Křížkovského 511/8 779 00 Olomouc, Czech Republic
E-mail: miroslav.medved@umb.sk; giorgio.zoppellaro@upol.cz; radek.zboril@upol.cz; michal.otyepka@upol.cz

 The ORCID identification number(s) for the author(s) of this article can be found under <https://doi.org/10.1002/smll.202206587>.

© 2023 The Authors. Small published by Wiley-VCH GmbH. This is an open access article under the terms of the Creative Commons Attribution License, which permits use, distribution and reproduction in any medium, provided the original work is properly cited.

DOI: 10.1002/smll.202206587

Š. Kment, A. Bakandritsos, R. Zbořil
Nanotechnology Centre
VŠB – Technical University of Ostrava
17. listopadu 2172/15 708 00 Ostrava-Poruba, Czech Republic
M. A. Thottappali
Institute of Macromolecular Chemistry of the CAS
Heyrovského nám. 2 162 06 Prague 6, Czech Republic
M. Medved
Department of Chemistry
Faculty of Natural Sciences
Matej Bel University
Tajovského 40 974 01 Banská Bystrica, Slovakia
M. Otyepka
IT4Innovations
VŠB – Technical University of Ostrava
17. listopadu 2172/15 708 00 Ostrava-Poruba, Czech Republic

contain other light elements, for example, oxygen and nitrogen, included as local dopants and/or functional groups located on the nanoparticle's surface. Experimental and theoretical studies demonstrated that the unique PL properties of CDs are mostly associated with the sp^2 carbon core states ($\pi-\pi^*$ transitions) and surface or core-surface states linked to the presence of functional groups on the CDs shell such as $-SH$, $-NH_2$, $C=O$, $COOH$, $-C=N-$ and $-CN$.^[38–45] The core-surface interactions and the emergence of solvent effects (polar vs nonpolar interactions, H-bonds) are phenomena that can substantially modulate radiative, as well as non-radiative processes, including the light absorption and emission characteristics (band profiles and emission lifetimes) in solution.^[14,42,46] Beyond the PL properties,^[47,48] the upfront application of CDs in photocatalysis remains difficult to realize.^[49] One key aspect to resolve is the CDs' photoactivation ability to form—via electron transfer processes—long-living polaron states and charged separated species that do not undergo fast recombination. Such properties can be imprinted in the material by introducing structural defects via surface oxidation, surface passivation, elemental doping (e.g., with light and/or heavy elements), or by surface functionalization with selected molecules that act specifically as electron donor or electron acceptor sites.^[50–54] However, there is no clear design that allows to clearly anticipate the possible generation of excited states (ESs) in CDs that are potentially useful in photocatalysis.^[45,55,56] In this work, we introduce the concept of spatial anisotropy as the key factor for the synthesis of multifunctional (optically and photocatalytically active) carbon-based nanomaterials and demonstrate that Asp-CDs give, under light excitation, not only highly emissive PL units but also express long-living magnetic electron/hole polaron species. Such features result from the spatial organization of Asp-CDs, which is interpreted in terms of a two-domain structure, a hydrophobic carbon-rich region (core) and a hydrophilic region (shell) that contains a larger amount of oxygen and nitrogen atoms. The multidomain architecture naturally favors charges and spin separation (electrons, e^- , and holes, h^+) without further additions of defects structures, introduced by post-synthetic procedures. We analyzed experimentally and theoretically in detail the PL properties of Asp-CDs and showed that different types of solvents (water, water/2-propanol mixture) can substantially modulate both the photophysical behavior (PL properties) and the magnetic polarons distribution (e^-/h^+), affording a combination of charged separated domains, magnetically non-interacting, and exchanged coupled triplet states ($S = 1$). In Asp-CDs, core and shell regions, following photoexcitation, exhibit well-recognizable electronic fingerprints (core: sustained PL in water (solid phase, $T = 220$ K); sharp isotropic resonant signal vs shell: quenched PL in water (solid phase, $T = 220$ K); formation of asymmetric wings), as unveiled from PL spectroscopy and electron paramagnetic resonance experiments. Using in situ light-induced electron paramagnetic resonance spectroscopy (X-band LEPR), the observed characteristic resonance signals of e^-/h^+ were interpreted in terms of $S = 1/2$ centers associated with electrons residing on C sp^2 regions (e^-) and $S = 1/2$ holes located on N and O richer regions (h^+). These sites behaved as spatially separated magnetic polarons; the presence of interacting through-space e^-/h^+ sites resulted in spin-coupled systems and the concentration of interacting

$S = 1$ centers was sensitive to medium polarity. The generation of photoexcited $S = 1$ states (following Asp-CDs photoexcitation at 325 nm) was enhanced in benzene and admixture of water/2-propanol, whilst decreased in pure water (pH = 7). Therefore, the Asp-CDs material behaves as an organic photoemitter in which polaron and triplet states generated by intersystem crossing (ISC) are tweaked by solvent interactions. We further exploited these photoinduced spin-separated species for the photoproduction of H_2O_2 , which is a high-energy oxidant, important in various fields ranging from medicine, and chemical industry to environmental technologies.^[57–60] Interestingly, the Asp-CDs generated H_2O_2 even without the presence of oxygen, unlike other sole CD photocatalysts.^[61] Theoretical calculations established a link between structural features and photoexcitation processes in Asp-CDs, which corresponded well with experimental observations. These findings can be taken as a blueprint for the rational design of carbon-based photocatalysts.

2. Results and Discussion

Highly emissive Asp-CDs were prepared by a solvothermal method, using aspartic acid as the sole chemical precursor (Figure S1a, Supporting Information) according to the published protocol.^[32] Detailed structural analysis of prepared Asp-CDs is provided in Supporting Information (Figures S1–S4, Supporting Information). The results confirm that the synthesized Asp-CDs material shares similar size distribution, chemical composition, and structural organization to the CD materials reported earlier.^[32] Furthermore, the structural analysis suggest that Asp-CDs consist both of a highly carbonized core (fragments of π -conjugated sp^2 carbon domains) and a hydrophilic surface. Thus, the arrangement of Asp-CDs into a two-domain structure in a virtual core/shell fashion can be envisaged.

To probe the electronic fingerprints of the Asp-CDs system and to unveil the emergence of different excited states radiative relaxation pathways associated with its predicted core/shell organization, the optical properties of Asp-CDs dispersed in water were examined by absorption and PL spectroscopies (Figure S5, Supporting Information). Asp-CDs exhibit a broad visible absorption range with a specific feature centered around 355 nm (Figure S5, Supporting Information, black line). Absorption bands in this range are typically ascribed to surface-exposed groups and molecular fluorophores. On the other hand, absorption in the high-energy region (<300 nm) can be associated with $\pi-\pi^*$ transition occurring mainly in sp^2 carbon domains (core region). Thus, the presence of these two bands in the absorption spectrum indicates the existence of the optically active transitions related to the graphitic core and surface-exposed groups containing O, N in Asp-CDs.^[40,45,54] The excitation wavelength range of the Asp-CDs extends from 285 to 445 nm with a PL excitation maximum centered at 355 ± 2 nm (Figure S5, Supporting Information, blue line) aligning with the position of the absorption band corresponding to the surface and/or molecular states. Intense blue emission occurs under optimal excitation of 355 nm with the PL emission maximum centered at 450 nm (Figure S5,

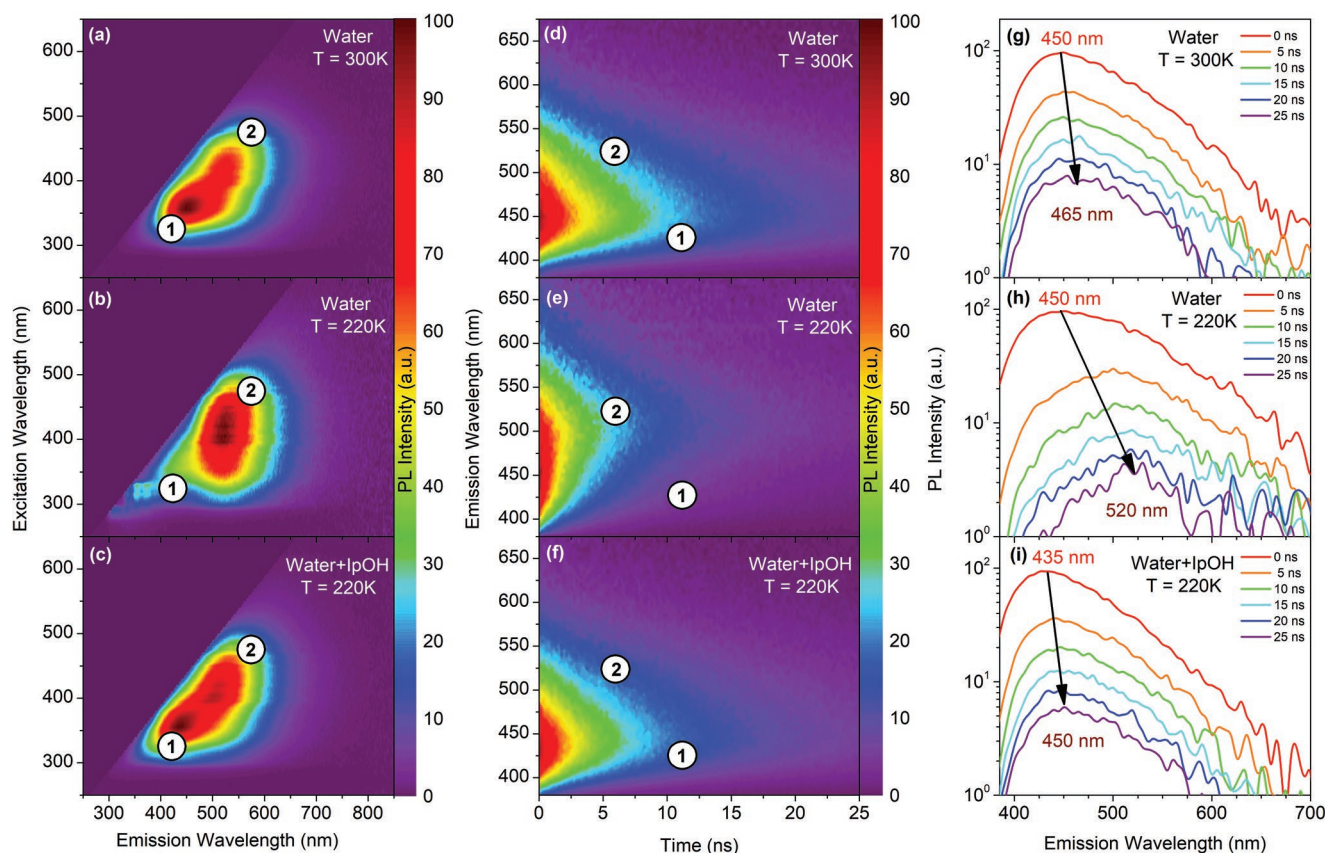


Figure 1. Influence of liquid-to-solid (water-to-ice) phase transition on steady-state and time-resolved PL of Asp-CDs. a–c) Excitation-emission color maps of Asp-CDs; in liquid phase, $T = 300$ K (a); solid phase, $T = 220$ K (b), and in solid phase after the addition of 2-propanol, $T = 220$ K (c) with individual PL emission centers labeled. d–f) Time-resolved PL emission color maps with extracted time-resolved emission spectra g–i) of Asp-CDs measured at the same conditions (phase, temperature, solvent) as in the steady-state experiments under 372 nm excitation.

Supporting Information, green line). Room temperature PL excitation-emission mapping was then performed to gain additional knowledge on the core/shell organization of Asp-CDs. Besides the dominant PL emission center located at 450 nm (center 1), an additional center positioned at 520 nm (labeled as center 2) arose under its optimal excitation at 420 nm (Figure 1a). To rule out the presence of unbound molecular fluorophores, which could affect the overall PL properties of CDs, excitation-emission maps of Asp-CDs before and after dialysis (Figure S6a,b, Supporting Information), as well as size-exclusive column chromatography (Figure S6c, Supporting Information), were acquired, showing that the PL properties of CDs remained unchanged after these purification procedures, which confirms that emission from center 1, as well as center 2, can be attributed solely to the Asp-CDs system. Recently, it was reported that a water-to-ice phase transition of the citric acid-based CD dispersions leads to quenching of fluorescence originating from the molecular fluorophores attached to the surface of the synthesized CDs due to the formation of charge-separated CD core-shell trap states.^[14] Since results from structural analysis predict similar virtual core-shell structures for Asp-CDs, the same methodology was applied to probe individual PL emission centers in Asp-CDs. Excitation-emission map of Asp-CDs dispersed in water (solid phase, $T = 220$ K) shows that fluorescence from center 1 is quenched, while center 2 remains

active (Figure 1b). Considering that the hydrophilic CD surface is in close contact with the solvent molecules, it is expected that its electronic fingerprints become more affected by interactions (e.g., electrostatic, H-bonding) compared to the shielded CD core region, in agreement with the findings revealed by molecular dynamics (MD) simulations for the citric acid based CDs.^[14] Following this principle, center 1 represents the PL properties of the CD surface, while center 2 corresponds to the properties associated with the CD core. To analyze the fluorescence quenching in Asp-CDs, spectrally and time-resolved PL (TR-PL) emission maps in these two phases (pure water and water/2-propanol mixture) were obtained in the spectral range 380 to 675 nm under the excitation at 372 nm. TR-PL maps (Figure 1d,e) indicate the strong dependence on the phase of the solvent in the 380–475 nm spectral region (center 1). On the other hand, the TR-PL signal collected in the higher wavelength range (500–600 nm) seems to be unaffected by the water-to-ice phase transition (center 2). Moreover, PL decay curves of Asp-CDs in both liquid and solid phases were measured to quantify the PL quenching (Figure S7, Supporting Information). PL lifetimes of 5.1 and 6.3 ns, corresponding to centers 1 and 2, respectively (liquid phase, $T = 300$ K), were extracted using a stretched-exponential function (see Experimental Section for more detailed information in Supporting Information) and fitting analysis (Figure S7a,b, Supporting Information). After

the liquid-to-solid phase transition occurred, a strong decrease in the PL lifetime of center 1 from 5.1 to 1.5 ns was observed (Figure S7c, Supporting Information), while the PL lifetime of center 2 remained less affected by the solvent phase change (Figure S7d, Supporting Information). To study the emission dynamics of both PL centers, TR-PL spectra before and after the water-to-ice phase transition were analyzed (Figure 1g,h). Passing the liquid-to-solid phase transition resulted in a significant increment of the quenching rate in the 380–475 nm spectral region (Figure 1h), giving a much larger spectral shift of ≈ 70 nm in the overall TR-PL spectra (compared to ≈ 15 nm measured in a liquid phase). This phenomenon is thought to arise from phase transition-induced activation of nonradiative relaxation channels.^[14] The addition of 2-propanol to the Asp-CD aqueous dispersion prevented the quenching of fluorescence originating from the CD surface states (center 1) during the liquid-to-solid phase transition. Both steady state (Figure 1c) and time/spectrally-resolved (Figure 1f) PL maps of Asp-CDs dispersed in the water/2-propanol mixture (50:50 vol%) at 220 K show similar features as those measured in pure water (liquid phase) at 300 K. PL lifetime of center 1 recovered 80% of its initial value (Figure S7e, Supporting Information), and the spectral shift in TR-PL reached similar value (≈ 15 nm) after 25 ns as that witnessed in the liquid phase (water) measurements (Figure 1i). These results indicate that after the addition of 2-propanol, the radiative relaxation from emission center 1 is the preferred radiative energy-releasing process,

even in the solid phase. The PL spectroscopy results clearly show that the complex PL emission of Asp-CD can be understood by invoking the presence of a virtual core/shell structural organization. Moreover, such morphology of CDs can induce a difference in electron affinity between the core and the shell domains, which can lead, besides the formation of excitons, to the generation of highly reactive charge-separated carriers, capable to sustain redox reactions.

In order to observe the existence of long-living photo-generated spin active states in Asp-CDs, the LEPR technique was employed. Due to the fast recombination rates of spin couples (polaron pairs, $\tau \approx$ ps) at room temperature, the generation of photoexcited spin active states in Asp-CDs was studied in a frozen matrix solution ($T = 80$ K). Under dark conditions, EPR spectra of Asp-CDs are nearly EPR silent, thus the material contains a negligible number of paramagnetic sites ($\ll 10^{18}$ spin/g) (Figure S8, Supporting Information). However, upon UV irradiation (@325 nm), a strong resonance signal around $g \approx 2.00$ becomes well resolved in the EPR spectrum, which indicates the formation of spin-active species characterized by lifetimes long enough to become EPR observable ($T = 80$ K). For comparison, the EPR signals obtained under UV light of Asp-CDs dispersed in water, water/2-propanol mixture (50:50 vol%), and benzene solutions are shown in Figure 2a–c. The estimated spin-spin relaxation time (T_2) evaluated for the narrow and slow relaxing $g \approx 2.00$ resonance spin component, $T_2 = 2/\sqrt{3} \times [\hbar / (g \times \beta_e \times \Delta B_{pp})]$, is 9.4 ns (see, Figure S9, Supporting

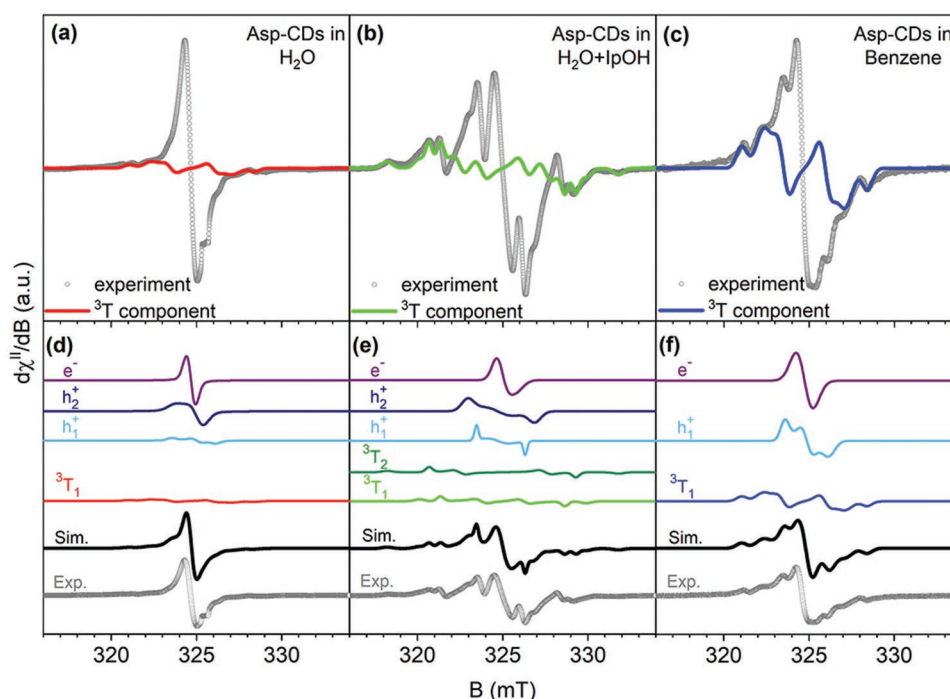


Figure 2. X-band light-induced EPR (LEPR) spectra of photogenerated charges in Asp-CD/solvent. a–c) LEPR envelopes of Asp-CDs in water, water/2-propanol (50:50 vol %), and benzene solutions. Experimental data are presented as gray symbols, whereas the $S = 1$ (3T) spin components are presented as red, green, and blue lines, respectively. Experiments were performed at $T = 80$ K and under in situ UV irradiation (@325 nm, 200 mW). d–f) EPR simulations of the various spin components of Asp-CDs as observed in water, water/2-propanol (50:50 vol %), and benzene solutions. Experimental data are presented as gray symbols, whereas the sum of all simulated spin components is given as black lines. The diverse spin species resulting from simulation coded as electron (e^-), hole (h^+), and triplet (3T) species are drawn with red, dark and light green, light and dark blue, navy, and purple lines, respectively.

Information, for details). The observed variance in the LEPR resonances and signal shapes indicate formation in Asp-CDs of charged separated electron (e^-) hole (h^+) paramagnetic species with relative concentrations dependent on the solvent's chemical nature. To interpret the observed EPR signals, computer simulations of the resonance envelopes for the e^-/h^+ and spin-coupled components were performed in the spin-Hamiltonian framework, $\hat{H} = \beta_e g \hat{S}_{a,b} B_0 - 2J\hat{S}_a\hat{S}_b + D[S_z^2 - \hat{S}(\hat{S}+1)/3] + E(S_x^2 - S_y^2)$. In \hat{H} , the terms D and E indicate the axial and rhombic zero-field-splitting, respectively, and J is the exchange-interaction energy between spin-coupled electron (e^- , \hat{S}_a) and hole (h^+ , \hat{S}_b) sites. In Figure 2a, the sharp isotropic resonant signal falling at $g_{\text{iso}} = 2.000$ (around 325 mT resonance magnetic field) corresponds to electrons located in sp^2 carbon-rich domains and accounts for 39.4% of the total (EPR detectable) spin density. The regions containing heteroatoms (N, O centers) give hole signatures (h^+ sites) that produce asymmetric wings developing from the strong $g = 2.000$ resonance line. The resonance signals due to the hole centers could only be simulated (Figure 2d) by invoking overlapped contributions of two species, one axial with $g_z = 2.005$ and $g_{x,y} = 1.996$ (marked as h_2^+ , 38.4% of the total spin density), and a second spin component with rhombic distortion (labeled as h_1^+), with $g_z = 2.004$, $g_y = 1.998$, and $g_x = 1.992$ (11% of the total spin density). Other weaker signals are assigned to magnetic interactions arising between e^- and h^+ sites, giving triplet states (3T_1) characterized by $g_{x,y,z} = 2.000$, $D = 3.7$ mT, $E/D \approx 0.1$, and $J < 7$ cm^{-1} . The calculated $S = 1$ resonance feature highlighted by the red spectrum is shown in Figure 2a (11.2% of the total spin density). We suggest that the h^+ centers in Asp-CDs are bulk exposed and the surface disorder, arising from an uneven spatial distribution of N and O-rich regions, translates into a variance in the EPR signals. Furthermore, under the framework of the magnetic point-dipole approach,^[62] the calculated D value provides an estimation of the through-space distance of the magnetically interacting spin species ((e^-, \hat{S}_a) and hole (h^+, \hat{S}_b)) of ≈ 0.9 nm; this value is compatible with a core-shell representation of spin domains consistent with the observed averaged nanoparticle's dimension of 2.5 nm, as given earlier. From these observations, it is anticipated that the hole centers, if truly bulk exposed, should exhibit higher sensitivity to changes in the environment, thus sensitive to interactions with solvent molecules, contrary to the shielded electrons located onto the nanoparticle's core.

The ability of the Asp-CDs system to deliver e^- to an acceptor molecule was probed in water upon the addition of methylviologen (MV). Following in situ UV irradiation @325 nm ($T = 260$ K), fast formation of the EPR resonance signal clearly associated with methylviologen radical cation ($MV^{+\bullet}$) was observed. The experimental EPR spectrum of the so-formed $MV^{+\bullet}$ is given in the Supporting Information (Figure S10, Supporting Information). To test the presence of any dependence of the electronic features associated with the spin-active photoexcited species upon changing the solvent, LEPR experiments were performed on Asp-CDs dispersed in a water/2-propanol (50:50 vol%) mixture, as well as in benzene. The recorded LEPR spectrum under UV-light irradiation for the water/2-propanol mixture and the benzene solution is shown in Figures 2b and 2c, respectively. From spectrum analysis, the overall resonance line in the water/2-propanol mixture exhibits different features

compared to those seen in neat water, with significantly more pronounced signals coming from "surface-exposed" hole centers. Likewise, in the features recorded in water, only a small variance of the strong resonant line arising from the electrons confined in the core region is observed, at $g_{\text{iso}} = 1.992$ (27.2% of the total spin density), and the formation of two rhombic components associated to the hole sites (h_1^+) with $g_z = 2.010$, $g_y = 2.000$, $g_x = 1.999$ accounting for 13% of the total spin density and (h_2^+) giving $g_z = 2.007$, $g_y = 2.000$, $g_x = 1.990$, and 30.8% of the total spin density. The presence of mixed polar solvents (water/alcohol) leads to the development of an admixture of triplet states i) $g_{x,y,z} = 1.997$, $D = 6.8$ mT, $E/D \approx 0.09$ with 14.3% of the total spin density, with an estimated through-space distance of 0.74 nm, and ii) $g_{x,y,z} = 1.997$, $D = 4.9$ mT, $E/D \approx 0.16$ with 14.7% of the total spin density, giving an estimated through-space distance of 0.83 nm, with $J < 7$ cm^{-1} . The overall contribution to the EPR resonance line of these $S = 1$ species (29% of the total spin density) is given in the LEPR spectrum (Figure 2b, green line). For clarity, the entire spectra simulations of the various spin components in Asp-CDs in a water/2-propanol (50:50 vol%) mixture are shown in Figure 2e. These data indicate that the formation of separated polarons and magnetically interacting e^-/h^+ species is an intrinsic property of the as-synthesized Asp-CDs under photoexcitation, which is intimately associated to spin/charged separated species featuring an anisotropic space distribution of atomic elements C, N, and O. To validate further this picture, we performed LEPR power saturation experiments on Asp-CDs in water/2-propanol (50:50 vol%) mixture, and confirmed that the saturation trends of e^- , h^+ , and spin $S = 1$ coupled species saturate very differently under increasing microwave powers, being the e^- species the fastest saturating components, followed by h^+ and then by $S = 1$, the slowest power saturating species (full details are given in Figure S11, Supporting Information). The observed trend in microwave power saturation behavior is expected for the admixture of uncorrelated and spin-coupled organic-based radicals.^[63] We finally tested the presence of photoexcited spin species of Asp-CDs in benzene, a nonreactive and weakly polar solvent. The LEPR spectrum of the Asp-CDs/benzene mixture is shown in Figure 2c and exhibits identical fingerprints for the photoexcited electrons ($g_{x,y,z} = 2.000$, 23.5% of the total spin density), but only one set of hole centers ($g_z = 2.006$, $g_y = 1.998$, and $g_x = 1.990$, 23.5% of the total spin density), and one set of $S = 1$ specie ($g_{x,y,z} = 2.000$, and $D = 3.7$ mT, $E/D \approx 0.11$, 53.0% of the total spin density, estimated through-space distance of 0.9 nm, $J < 7$ cm^{-1}). The computer simulations of these spin components are given in Figure 2f. Furthermore, we performed in situ measurements recording the time evolution of the LEPR signals of the spin active photoexcited species detected in Asp-CDs in water and water/2-propanol mixture. The resulting 2D color maps and 3D LEPR spectra are given in Figure 3. We employed for such purpose a light-off to light-on and then light-off photoexcitation time sequence. The results clearly highlight that the formation of the spin active species immediately follows the light irradiation and furthermore indicate that in the water/2-propanol mixture (Figure 3b,d), a more complex spin system (combination of triplets, 3T_2 , and 3T_1) emerges during the light-on process (see Figure 2 for notations). These magnetic polaron states, clearly, are long-living species after light

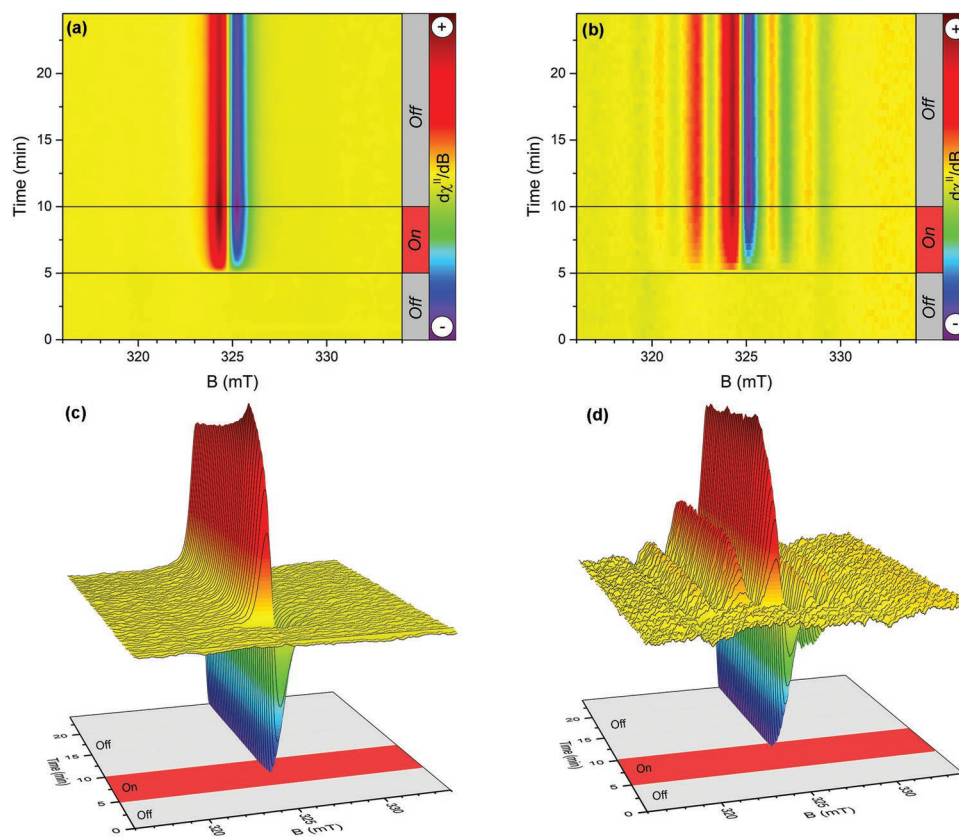


Figure 3. The 2D color maps (a,b) and 3D spectra (c,d) obtained from in situ LEPR experiment (CW X-band, 9.080 GHz, $T = 80$ K), showing the time evolution of the EPR signals when a dynamic light excitation sequence (off-on-off) is applied to the frozen systems of Asp-CDs in water (a, c) and water/2-propanol mixture (b,d). The following experimental conditions were used during measurements: sample kept under dark conditions (UV-off, signal acquisition time range 0–5 min) followed by in situ UV light exposure (UV-on, signal acquisition time range 5–10 min) and then back to dark conditions (UV-off, signal acquisition time range 10–25 min). The color coding in (a,b) indicates positive (+, red) to negative values (–, blue) of the EPR signal intensity ($d\chi''/dB$).

irradiation is cut off, at least true at 80 K. The occurrence of polaron states (e^-/h^+) and long-lived triplet states in Asp-CDs, which are formed during photoexcitation, supports the idea that in addition to engineering the chemical composition, band gaps, and structural properties, such as nanosystem size and shape, engineering the anisotropy of the system in the material is also crucial for applications in photocatalytic processes.

To understand the relationships between the unique structure and optical properties of Asp-CDs dispersed in water, as well as to elucidate the formation of polaron states, charge-separated species and triplet states in Asp-CDs irradiated by UV light as observed in the LEPR experiments, density functional theory (DFT) and its time-dependent formulation (TD-DFT) were employed in a thorough analysis of the electronic absorption/emission spectra and character of singlet/triplet excited states of an extended series of neutral and ionized model systems (Figure S12, Supporting Information). The model systems were carefully designed based on available experimental information (i.e., the elemental composition, the presence of carboxylic groups, as well as remnants of succinimide moieties in an O/N-rich surface region surrounding an sp^2 -carbon-rich core, as evidenced in high-resolution transmission electron microscopy (HRTEM) images)^[32] and followed a conceptual multi-layer model of Asp-CDs (Figure 4a) containing flakes of

various size: small ones (≈ 1.6 nm) on the CD “poles,” medium-size ones (≈ 1.8 nm) at “tropics,” and large ones (≈ 2 nm) at the “equator”. The plausibility of such a model was also supported by MD simulations, which showed that the quasi-spherical CD structure was stable in the aqueous environment, and the flakes tend to aggregate preferably forming stacked structures (Figure 4b and Figures S21 and S22, Supporting Information). First, the electronic structure of Asp-CD monolayers as a function of the size and surface functionalities was analyzed. As already mentioned, the optical properties of CDs result from an intricate interplay of core–core and core–surface electronic transitions. In general, we found that the absorption spectra of Asp-CDs were predominantly influenced by the flake size owing to the quantum confinement effect.^[64] The core–surface transitions typically occurred in the short-wavelength region (350–450 nm), whereas the core–core (π – π^*) absorption bands spread toward longer wavelengths with gradually decreasing intensity (Figures S14 and S16, Supporting Information). The surface groups were usually partly involved in delocalized π – π^* transitions, but neither the deprotonation nor the number of functional groups significantly affected the absorption spectra. On the other hand, the presence of edge N atoms often introduced new low-lying excited states shifting the absorption bands even to the IR region, in line with previous works.^[65] The observed

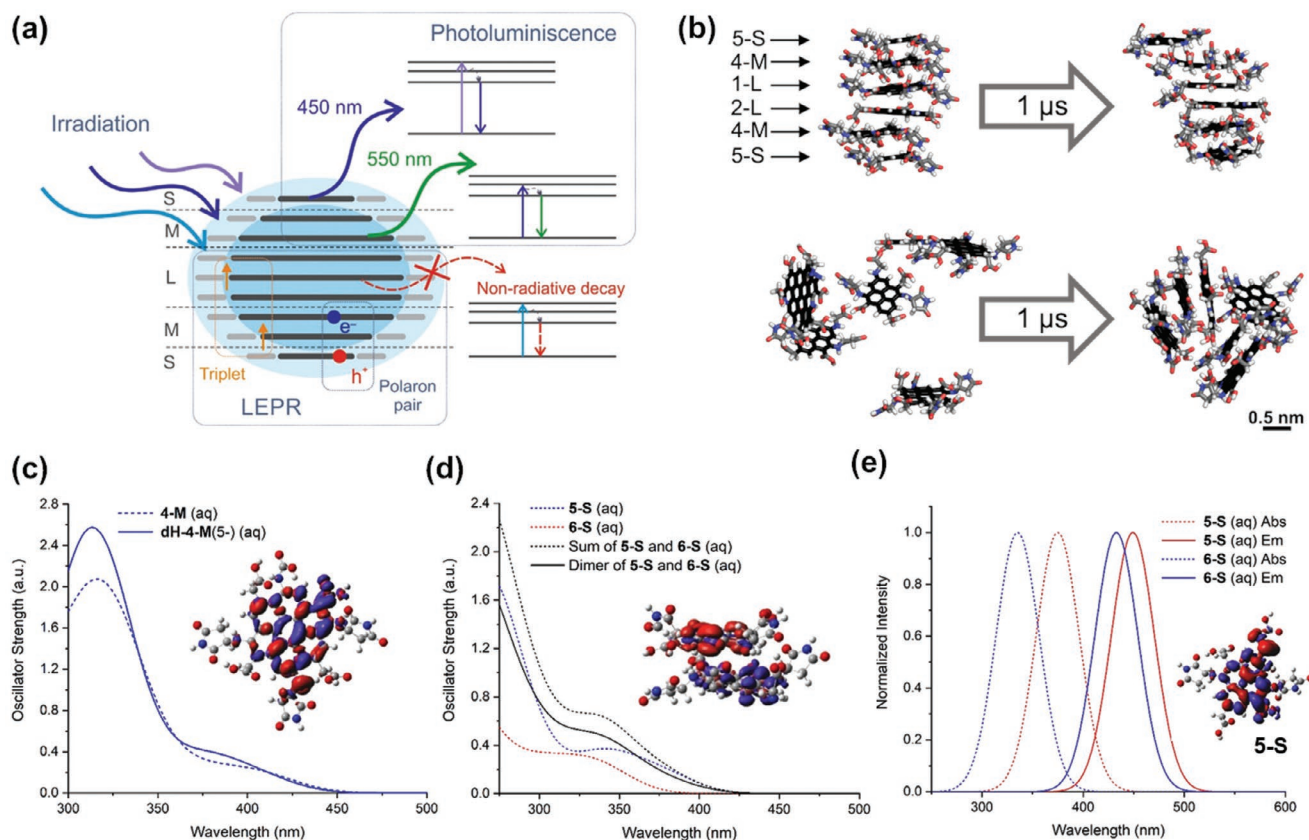


Figure 4. a) Cross-section of a conceptual multilayer model of a quasi-spherical Asp-CDs nanoparticle featuring a two-domain structure consisting of a hydrophobic core (deep sky blue) and a solvent-sensitive hydrophilic shell (light blue) with a schematic illustration of considered photophysical processes evidenced by PL and LEPR experiments. Inner π -conjugated carbon regions and flexible functionalities rich with heteroatoms in small (S), medium (M), and large (L) layers are represented by horizontal black and gray bars, respectively. b) Initial and final structures of MD simulations showing the stability and aggregation of CD layers (5-S, 4-M, 1-L, and 2-L correspond to specific small, medium, and large model structures; see Figure S12, Supporting Information). The color coding: carbon – gray/black, oxygen – red, nitrogen – blue, and hydrogen – white. Water is omitted for clarity. c) Simulated absorption spectra of protonated 4-M and deprotonated dH-4-M(5-) models in water. d) Absorption spectra of a stacking complex formed of 5-S and 6-S in water. e) Normalized absorption and emission bands corresponding to the $S_0 \rightarrow S_1$ transition in 5-S and 6-S in water obtained at the M06-2X/6-31+G(d)/SMD(water) level of theory. Insets: EDD plots for the $S_0 \rightarrow S_1$ transition (red/blue regions indicate decrease/increase of the electron density upon the excitation).

continuous decrease of the absorption curve (Figure S5, Supporting Information, black line) results from a heterogeneous character of the layers exhibiting multiple overlapping absorption bands with decreasing intensity for longer wavelengths (see Supporting Information for more details). Although the size of large and medium models did not allow us to theoretically study their emission spectra, it was reasonable to assume that the S_0 - S_1 gap would be reduced via the relaxation of the S_1 state. Also, owing to the vicinity of excited states, the breaking of the Kasha rule was not expected. As large layers and medium flakes containing edge N atoms featured low-lying S_1 states (absorption in the 900–1300 nm), we assumed that the photoexcitation of such systems ended up with a non-radiative decay to the ground state (GS). The observed long- and short-wavelength PL emission centers (Figure 1) could then be ascribed to the core–core transitions in medium-size layers without edge N atoms (such as model 4-M, Figure 4c and Figure S18c, Supporting Information) and small flakes (such as models 5-S and 6-S, Figure S19, Supporting Information) on the CD poles, respectively. Importantly, the electron density difference

(EDD) plots for the latter indicate that transitions have a strong charge-transfer (CT) character and thus can be sensitive to the environment. For the smallest models, the simulated emission spectra were consistent with the short-wavelength PL band peaking at 450 nm (Figure 4e). Interestingly, the multilayer structure of Asp-CDs implies the possibility of interlayer transitions. Whereas the consideration of such transitions would not change the proneness of large flakes toward non-radiative deactivations, they can play an important role in core–surface excitations. Indeed, the analysis of a stacking complex made of small flakes (5-S and 6-S, Figure S13, Supporting Information) showed that although the absorption band at 350 nm of the complex was very similar to the sum spectrum of individual components (Figure 4d), the $S_0 \rightarrow S_1$ transition had strong interlayer CT character involving the electron transfer from a smaller layer to the larger one.

Our theoretical picture is also consistent with the interpretation of the LEPR measurements described above. In particular, the majority of model systems (including the stacking complex) exhibited very low singlet-triplet splitting values (typically

$<2 \text{ kcal mol}^{-1}$) typically between the 1S_1 and 3T_3 states (Figures S15, S17, S18b,d, S19b,d, and S20b, Supporting Information). Although the vicinity of levels does not solely imply the efficiency of the ISC, it can be anticipated that such processes are plausible under continuous irradiation of samples by UV light. While in large flakes, fast non-radiative deactivation processes can effectively compete with the formation of long-lived triplet states, in the medium and small systems, spin species accumulate at the core–surface boundary (see, e.g., Figures S18b,d and S19b,d, Supporting Information), which can explain the interactions of surface spins observed in LEPR. Importantly, the findings for the stacking complex, namely that the lowest triplet state (like the lowest singlet) exhibits CT character involving the creation of an h^+ -site on a smaller (i.e., outer) layer and an e^- site on the larger (i.e., inner) one (Figure S20c,d, Supporting Information), are in keeping with the observed formation of polaron pairs in the LEPR experiments.

All in all, we found the proposed multi-layer “Earth-like” model of Asp-CDs (Figure 4a) fully consistent with the strong experimental evidence of the multicenter and environment-sensitive character of PL, as well as the formation of polaron states, charge-separated species, and triplet states in Asp-CDs upon pho-

toexcitation, thus not only providing indispensable insights into the physical mechanisms of such photoactivation processes but also vice versa, confirming the validity of the suggested model.

To further explore the nature of photogenerated magnetic polaron species and their application in the field of photocatalysis, LEPR measurements on Asp-CDs in the presence of *N*-tert-butyl- α -phenylnitron (PBN) spin trap were conducted (Figure 5a). The LEPR spectra obtained upon reacting under light irradiation at 325 nm (10 min, N_2 atmosphere, RT) of Asp-CDs with PBN in water solution revealed the formation of a radical signal with resonance pattern fully consistent with the PBN trap of hydroperoxyl radicals (HOO^\bullet , formation of PBN-OOH adduct) (hyperfine parameters from computer simulation: $A_N = 1.45 \text{ mT}$, $A_H = 0.28 \text{ mT}$). The result indicates the promising use of Asp-CDs as photocatalysts for H_2O_2 production from water. The photocatalytic activity of Asp-CDs was studied in water and water/2-propanol mixture (50:50 vol%) at room temperature and under air atmosphere. Asp-CDs dispersed in water were able to generate H_2O_2 with reaction rates of 140 and $52 \mu\text{mol g}^{-1} \text{h}^{-1}$ under UV light (365 nm) and one sun irradiation, respectively. The H_2O_2 production rates were further enhanced by the addition of 2-propanol to the reaction mixture,

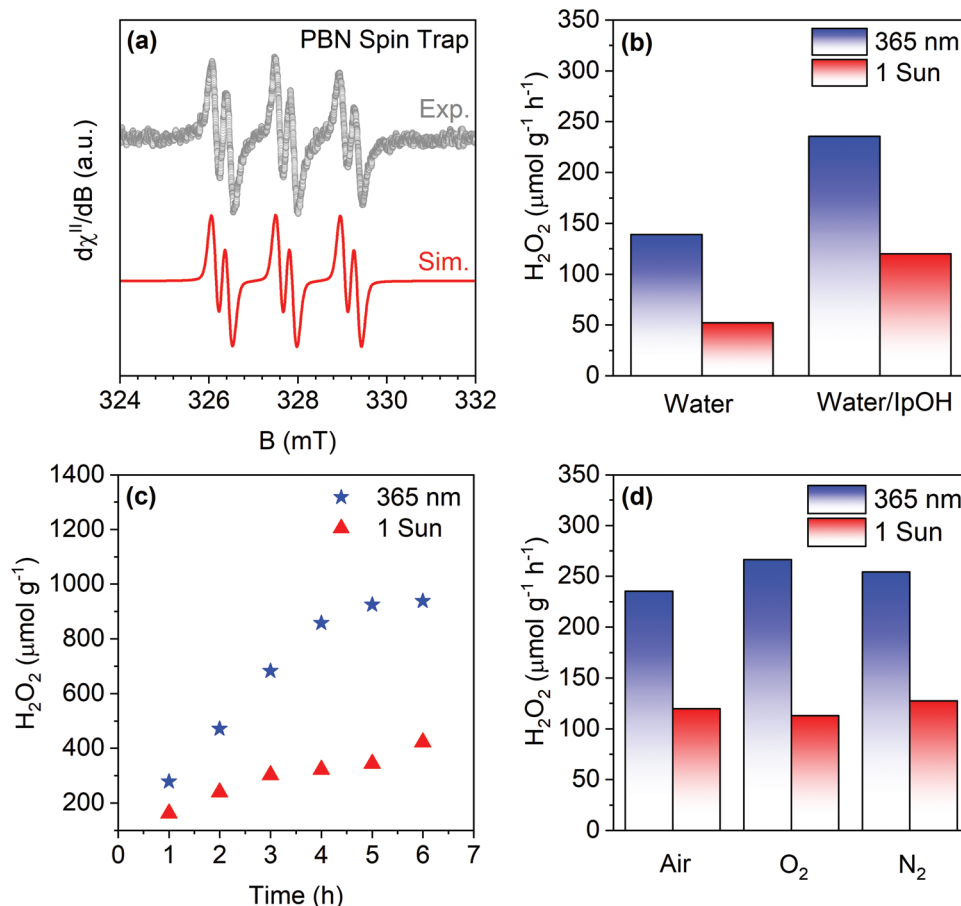


Figure 5. Photocatalytic production of H_2O_2 . a) PBN spin-trapping LEPR spectra (hydroperoxyl radicals) of Asp-CDs. Experimental data are presented as gray symbols, whereas the red line represents the computer simulation. b) H_2O_2 photoproduction rate of Asp-CDs in water and water/2-propanol mixture (50:50 vol%) for 2 h using UV (365 nm, 5 mW cm^{-2}) and solar light. c) Time-dependent profiles of H_2O_2 photoproduction by Asp-CDs in water/2-propanol mixture (50:50 vol%). d) H_2O_2 production rates of Asp-CDs in water/2-propanol mixture (50:50 vol%) under atmospheres of air, O_2 , and N_2 .

reaching the values of 240 and 120 $\mu\text{mol g}^{-1} \text{h}^{-1}$, respectively (Figure 5b). The time-dependent profiles of H_2O_2 photoproduction by Asp-CDs under UV light and one sun revealed that the H_2O_2 concentration was sustained during several hours of irradiation (Figure 5c).

Given the abundance of seawater, the capability of Asp-CDs to photoproduce H_2O_2 in seawater and seawater/2-propanol mixture (50:50 vol%) was also tested, revealing the Asp-CDs photocatalytic activity of 135 and 208 $\mu\text{mol g}^{-1} \text{h}^{-1}$ under UV light (365 nm), respectively. Under one sun, the reaction rates were determined to be 37 and 126 $\mu\text{mol g}^{-1} \text{h}^{-1}$ in seawater and seawater/2-propanol mixture (50:50 vol%), respectively (Figure S23, Supporting Information).

To uncover the reaction pathway of the H_2O_2 formation by Asp-CDs, photocatalytic activities of Asp-CDs in a water/2-propanol mixture (50:50 vol%) under air, O_2 , and N_2 atmospheres were studied. It was found that the reaction rate of H_2O_2 photoproduction remained nearly independent of the reaction environment (air, N_2 atmosphere, O_2 atmosphere), an indication that H_2O_2 is primarily formed through a water oxidation reaction (WOR). This finding demonstrates that photogenerated holes in Asp-CDs are surviving the electron/hole recombination processes long enough to effectively react with water molecules. The hypothesis is further supported by the EPR analysis, which revealed different electron–hole localizations in the Asp-CDs structure, with the holes located mainly on the Asp-CDs surface while electrons being preferentially localized in the aromatic carbon-rich nanoparticle's core. To the best of our knowledge, this is the first example of neat CD material capable of H_2O_2 photoproduction via WOR without the need to use additional co-catalyst components for effective H_2O_2 photoproduction.^[9,61,66–69] To further elucidate if 2-propanol can affect Asp-CDs photocatalysis and to exclude the possibility of alcohol photo-reforming during H_2O_2 photoproduction, nuclear magnetic resonance (NMR) analysis of the samples (Asp-CDs in water/2-propanol mixture) taken before and after the reaction was carried out. Representative ^1H NMR spectra confirmed that 2-propanol remained intact throughout the whole process and no side product deriving from 2-propanol was observed (Figure S24, Supporting Information), indicating that 2-propanol played the role of the stabilizer of the magnetic polaron states in Asp-CDs formed during photoexcitation, and does not act as an additional reactant in the H_2O_2 production. Furthermore, no degradation of the Asp-CDs photocatalyst during turnover was observed, for example, as a result of the accumulation of unspent electrons during the water oxidation process. Taking into consideration the witnessed diverse performance of H_2O_2 photoproduction, which depended on the irradiation wavelength used (larger H_2O_2 production under UV light, smaller under 1 sun, Figure 5c), the effectiveness of the H_2O_2 production even in N_2 atmosphere, and the combined EPR results, we suggest the reaction mechanism depicted in Scheme S1, Supporting Information, as the effective pathway, supported by Asp-CDs, for the catalytic photoproduction of H_2O_2 from water. Upon photoexcitation, e^-/h^+ magnetic polarons are generated in Asp-CDs, which localize into diverse domains of the photocatalyst (Scheme S1, Supporting Information, step 1), with the holes more exposed to solvent molecules in the bulk, and electrons more localized in the nano-photocatalyst core. The

photogenerated holes fast react with the water molecules which are in contact with the Asp-CDs hydrophilic surface, providing an effective formation of H_2O_2 (step 2). Under light irradiation, a fraction of hydrogen peroxide disproportionate into hydroxyl radicals (step 3, OH^\bullet) which readily react with nearby H_2O_2 molecules, giving hydroperoxyl radical species (step 4, OOH^\bullet), which production was confirmed by the PBN spin trap experiments, and further evolve into H_2O_2 and O_2 (step 5). Finally, the locally formed O_2 molecules from step 5 act as acceptors for the photoexcited electrons (step 6), which were generated together with holes in step (1), forming H_2O_2 . The overall reaction for photocatalytic H_2O_2 production is finally given by Equation S7, Supporting Information, and highlights that the local anisotropy in Asp-CDs is the key factor that gates the effective and cooperative use of both photogenerated electron/holes polarons, affording a single catalytic unit, without the need of co-catalysts, for driving water oxidation processes.

3. Conclusion

Beyond the tunable PL properties and besides the application of CDs as prime components in optoelectronic devices,^[11] the light-harvesting ability of these systems has the great potential to boost photocatalytic processes, either as photosensitizer and/or to become effective photocatalysts themselves.^[13] Although very appealing, unlocking such features in CDs remains difficult to realize from the synthetic point of view. It requires detailed knowledge of the nature of the photoactivated states, to understand the electronic factors that translate into stabilization of the photoexcited charges and formation of long-lived holes on the CDs surface. In this work, we have shown that the structural organization is the key factor that drives the emergence of magnetic polaron states upon photoexcitation in Asp-CDs. Asp-CDs can be seen as a two-domain multilayer nanodot assembly, ordered in a virtual core/shell fashion, which consists of a highly carbonized core (fragments of π -conjugated sp^2 carbon domains) and a hydrophilic surface, containing a high amount of oxygen and nitrogen-containing functional groups. The core and shell regions exhibit very different PL properties, also reflected in their PL response to polarity changes in the solvent medium, and these optical differences mirror the spatial anisotropic organization of the materials into distinct domains. The core/shell structure of Asp-CDs and the nature of the charge-separated species generated under photoexcitation have been validated by in situ LEPR spectroscopy, by using UV irradiation @325 nm. Moreover, the presence of defined fingerprints associated with photoexcited electron (e^-), hole (h^+) species, and spin-coupled systems (triplets, ^3T) was confirmed. The relative concentrations of these spin states, e^- , h^+ , and stabilization of ^3T were found to depend on the solvent's chemical nature and polarity of the solvent; the e^-/h^+ spin coupling giving ^3T states became more effective in benzene, followed by water/2-propanol mixture and least in neat water. Theoretical analysis based on (TD-)DFT calculations and MD simulations performed on model systems, which were visualized as multi-layer quasi-spherical assemblies containing stacking flakes of various sizes, demonstrated that the optical properties of Asp-CDs result from an intricate interplay of core–core and core–surface electronic transitions, exhibiting very low

singlet-triplet splitting values (typically <2 kcal mol⁻¹), between the singlet (¹S) and triplet (³T) states. Large domains undergo fast non-radiative deactivation processes, which can effectively compete with the formation of long-lived triplet states, whereas medium and small-size domains show that the spin species accumulate at the core–surface boundary. In addition, we exploited the formation of magnetic polaron states in Asp-CDs for H₂O₂ photoproduction via WOR. Sole Asp-CDs were able to produce H₂O₂ in pure water even without the presence of oxygen, and a further enhancement in H₂O₂ reaction yield was achieved when 2-propanol was introduced into the reaction mixture, confirming its role as a stabilizing agent for photocatalytically active states. The observed formation of long-living magnetic polaron states in Asp-CDs, resulting from their spatial organization, underlines the vast potential of carbon-based nanomaterials in the field of photocatalysis.

4. Experimental Section

Chemicals and Reagents: All chemicals were supplied by Sigma-Aldrich and used without further purification unless otherwise stated. Absolute ethanol (99.5%+) was purchased from VWR Chemicals. Dialysis tubing (2 kDa cut-off, benzoylated) for colloid purification was purchased from Sigma-Aldrich.

Synthesis of Asp-CDs: Asp-CDs were produced by a solvothermal method according to a previously published protocol.^[32] Briefly, 500 mg of aspartic acid was mixed with 15 mL of absolute ethanol and left in an ultrasonic bath for 30 min. The prepared suspension was processed by a solvothermal procedure in a Teflon-lined stainless-steel autoclave at 210 °C for 8 h. The solution was filtered using a 200 nm Teflon syringe filter and transferred to 20 mL of deionized water. The solution was then heated in a reaction flask at 40 °C for a few hours until the unwanted ethanol was eliminated. The obtained aqueous colloidal suspension of Asp-CDs was again passed through a syringe filter and then dialyzed against deionized water for 24 h to remove residual small molecular species. Size-exclusive column chromatography (PD MiniTrap G-25) was performed to confirm the high monodispersity of Asp-CDs.

Material Characterization: TEM images were acquired on a JEOL 2010 transmission electron microscope operating at 160 kV. XPS analysis was carried out using a PHI VersaProbe II (Physical Electronics) spectrometer with an Al K α source (15 kV, 50 W). The Fourier transform infrared (FT-IR) spectrum was collected on an iS5 Thermo Nicolet FT-IR spectrometer using the Smart Orbit ZnSe ATR technique.

Spectroscopy Measurements: The UV–vis absorption spectrum of the colloidal Asp-CDs was recorded on a Specord S600 spectrometer (Analytik Jena, Germany). Steady-state and TR-PL measurements were performed on an FLS980 fluorescence spectrometer (Edinburgh Instruments) equipped with a 450 W xenon arc lamp and EPL-375 ps pulsed diode laser ($\lambda_{em} = 372$ nm with a pulse width of 66.5 ps, a repetition rate of 10 MHz, and an average power of 75 μ W, also Edinburgh Instruments) as the excitation sources. PL decay curves were fitted using a stretched exponential function: $I(t) = I_0 e^{-(t/\tau)^\beta}$, where the fitting parameters τ and β are the PL decay time and stretch parameter, respectively. PL measurements of the samples in liquid and solid phases were conducted using a variable-temperature liquid nitrogen optical cryostat OptistatDN2 controlled by a cryogenic programmable temperature controller Mercury iTC (Oxford Instruments).

EPR Measurements: EPR spectra were acquired on a JEOL JES-X-320 spectrometer operating at X-band (≈ 9.14 – 9.17 GHz); EPR envelopes were collected at 80 K. The quality factor (Q) was maintained above 6000 for all measurements. High-purity quartz tubes (Suprasil, Wilmad, ≤ 0.5 OD) were used as a sample holder and the accuracy of the g -values was determined by comparison with a Mn²⁺/MgO standard (JEOL standard). The microwave power was set to 1.9 mW to avoid power saturation

effects. A modulation width of 0.35 mT and a modulation frequency of 100 kHz were used. All EPR spectra were collected with a time constant of 30 ms and a sweep time of 2 min with three accumulations to improve the signal-to-noise ratio. HeCd laser (325 nm, 200 mW) was employed as the UV light source during the EPR measurements fitted with a fiber optic cable directly into the cavity resonator dedicated window. All EPR spectra were simulated in the Matlab software platform; the EasySpin simulation package was used for spin-Hamiltonian simulations.^[70]

Computational Details: The GS structures of all monolayer model systems were optimized employing DFT at the M06-2X level^[71] using the 6–31G atomic basis set.^[72] The choice of the exchange–correlation functional was based on the fact that it performs well not only for the GS thermochemistry but also for the analysis of ESs.^[73] To better describe dispersion interactions, the ω B97X-D functional^[74] in combination with the def2-SVP basis set^[75] was applied for the geometry optimization of a two-layer model. In all cases, vibrational analysis was performed, and the absence of imaginary frequencies was checked to confirm the character of the stationary points on the potential energy surface. Solvent effects were accounted for by using an implicit Solvation Model based on Density (SMD).^[76] ESs were explored using TD-DFT employing the M06-2X functional with the 6–31+G(d) basis set. Whereas for the simultaneous analysis of multiple singlets, as well as triplet ESs, the SMD model was combined with the linear response (LR) approach, and the emission spectra were obtained state-specifically (for the S₁ \rightarrow S₀ transition) applying the recently proposed cLR² approach,^[77] which included the dynamical response of the solvent to the solute transition density, as well as a perturbative correction of the state-specific polarization of the solvent due to the ES density (cLR), and was shown to be superior to both LR and cLR for various types of transitions. All calculations were performed using the Gaussian16 program.^[78]

In MD simulations, a multicomponent hydrated system consisted of one 1-L, one 2-L, two 4-M, and two 5-S monolayer models parametrized in the Generalized Amber Force Field (GAFF)^[79] with refined parameters for aromatic carbon atoms.^[80] The geometries of 1-L, 2-L, 4-M, and 5-S were first optimized at the B3LYP/6-31G*^[81,82] level, and the electrostatic potentials at these geometries were calculated at the HF/6-31G* level in gas. RESP^[83] partial charges were assigned by the Antechamber tool^[84] from the Amber12 software package.^[85] Atom types, bond, angle, and dihedral parameters were assigned by tleap from the same package. Finally, a topology in Amber format was translated to Gromacs format using amb2gmx.pl script. To address the stability of the quasi-spherical organization of Asp-CDs and the feasibility of its formation, two cases with different starting positions were chosen. First, the monolayers were pre-stacked and solvated with TIP3P^[86] explicit water molecules (3889 in total) in the box of $5 \times 5 \times 5$ nm³ at the beginning of the simulation. Second, the monolayers were randomly placed in the simulation box and solvated with 3875 water molecules. After minimization, a two-step equilibration was carried out. First, the system was thermalized from 0 to 300 K for 1 ns with the V-rescale^[87] thermostat with a 0.1 ps scaling constant. Then, 2 ns equilibration of pressure was performed using the isotropic Berendsen barostat^[88] to keep the pressure at 1 bar during the simulation, the time constant for pressure relaxation was set to 2 ps, and the temperature was kept at 300 K. Productive 1 μ s long MD simulations were carried out under NpT conditions with a 1 fs time step, bonds involving hydrogen were constrained using the LINCS^[89] algorithm. The temperature was kept at 300 K with the V-rescale thermostat with a 0.1 ps scaling constant, the pressure was kept at 1 bar using the isotropic Parrinello–Rahman barostat,^[90] and the time constant for pressure relaxation was 1 ps. The electrostatic interactions were treated by means of the particle-mesh Ewald (PME)^[91] method with a real-space cutoff of 1 nm; the same cutoff was applied for van der Waals interactions. Periodic boundary conditions were applied in all three dimensions. All MD simulations were performed in Gromacs 5.0.^[92] Figures from the MD simulations were rendered in PyMOL.^[93]

Photocatalytic H₂O₂ Production: Photocatalytic H₂O₂ production experiments were carried out using a xenon lamp equipped with an AM1.5 G filter at one sun intensity (100 mW cm⁻²) and a UV LED (365 nm, with a power density of 5 mW cm⁻²) as an irradiation source.

Colloidal suspension of Asp-CDs was dispersed in a total of 6 mL of water and water/2-propanol mixture (50:50 vol %), respectively, with the resulting amount of photocatalyst set to 4.5 mg. A photometric Spectroquant H₂O₂ Test was used to quantify H₂O₂ production (at 450 nm, the detection limit in the range of 0.015–6 mg L⁻¹ H₂O₂). For photocatalytic measurements in a specific atmosphere, the suspension was continuously flushed with O₂ and N₂ before and during illumination for 15 min.

Nuclear Magnetic Resonance: ¹H NMR measurements were performed using a JEOL JNM-ECZ400R series with a superconducting coil having a magnetic field of 400 MHz (9.4 T). A water suppression technique was used to remove the water peak. D₂O (200 μL) was added to each sample before measurement. The NMR spectra were collected at room temperature, performing 16 scans, with a resolution of 16 384 points, and a relaxation delay of 5 s.

Supporting Information

Supporting Information is available from the Wiley Online Library or from the author.

Acknowledgements

The authors acknowledge the support from the Ministry of Education, Youth and Sports of the Czech Republic (CZ.1.05/2.1.00/19.0377) and the assistance provided by the Research Infrastructure NanoEnvCz, supported by the Ministry of Education, Youth and Sports of the Czech Republic under the Project No. LM2015073. The authors also acknowledge the support by the Operational Program Research, Development and Education – Projects No. CZ.02.1.01/0.0/0.0/15_003/0000416 and CZ.02.1.01/0.0/0.0/16_019/0000754 of the Ministry of Education, Youth and Sports of the Czech Republic. This work was supported by the Ministry of Education, Youth and Sports of the Czech Republic through the e-INFRA CZ (ID:90140). L.Z., M.L., and D.P. acknowledge the support from the Student Project IGA_PrF_2022_019. M.M. acknowledges the support from the Slovak Research and Development Agency (APVV-20-0098). This work was supported by the Ministry of Education, Youth and Sports of the Czech Republic through the e-INFRA CZ (ID:90140). G.Z. thanks the Czech Science Foundation (GACR, 22–26416S). The COST Action CA21101 is also acknowledged. M.A.T. acknowledges the support of the Czech Science Foundation (GACR, 22–02005S). Authors also gratefully acknowledge Jana Stráská, Martin Petr, and Lukáš Tabery for material characterization, and Dr. Kateřina Holá and Dr. Jiří Pflieger for scientific discussions.

Conflict of Interest

The authors declare no conflict of interest. A patent on this work is pending.

Author Contributions

L.Z. and Z.B. contributed equally to this work. The manuscript was written through the contributions of all authors. All authors have given approval for the final version of the manuscript.

Data Availability Statement

The data that support the findings of this study are openly available in ZENODO at <https://doi.org/10.5281/zenodo.7247083>, reference number 7247083.

Keywords

carbon dots, density functional theory, high spin species, hydrogen peroxide, photoluminescence, polarons, water oxidation

Received: October 25, 2022

Revised: March 17, 2023

Published online: April 10, 2023

- [1] S. S. Mao, S. Shen, *Nat. Photonics* **2013**, *7*, 944.
- [2] Q. Wang, C. Pornrunroj, S. Linley, E. Reisner, *Nat. Energy* **2021**, *7*, 13.
- [3] E. Romero, V. I. Novoderezhkin, R. van Grondelle, *Nature* **2017**, *543*, 355.
- [4] J. Liu, Y. Liu, N. Liu, Y. Han, X. Zhang, H. Huang, Y. Lifshitz, S.-T. Lee, J. Zhong, Z. Kang, *Science* **2015**, *347*, 970.
- [5] Y. Shiraishi, T. Takii, T. Hagi, S. Mori, Y. Kofuji, Y. Kitagawa, S. Tanaka, S. Ichikawa, T. Hirai, *Nat. Mater.* **2019**, *18*, 985.
- [6] Y. Shiraishi, S. Kanazawa, Y. Kofuji, H. Sakamoto, S. Ichikawa, S. Tanaka, T. Hirai, *Angew. Chem., Int. Ed.* **2014**, *53*, 13454.
- [7] H. Wu, H. L. Tan, C. Y. Toe, J. Scott, L. Wang, R. Amal, Y. H. Ng, *Adv. Mater.* **2020**, *32*, 1904717.
- [8] Y. Nosaka, A. Y. Nosaka, *Chem. Rev.* **2017**, *117*, 11302.
- [9] Y. Li, Y. Zhao, J. Wu, Y. Han, H. Huang, Y. Liu, Z. Kang, *J. Mater. Chem. A* **2021**, *9*, 25453.
- [10] S. Y. Lim, W. Shen, Z. Gao, *Chem. Soc. Rev.* **2015**, *44*, 362.
- [11] L. Wang, W. Li, L. Yin, Y. Liu, H. Guo, J. Lai, Y. Han, G. Li, M. Li, J. Zhang, R. Vajtai, P. M. Ajayan, M. Wu, *Sci. Adv.* **2020**, *6*, eabb6772.
- [12] K. Holá, Y. Zhang, Y. Wang, E. P. Giannelis, R. Zbořil, A. L. Rogach, *Nano Today* **2014**, *9*, 590.
- [13] B. Wang, S. Lu, *Matter* **2022**, *5*, 110.
- [14] S. Kalytchuk, L. Zdražil, Z. Bad'ura, M. Medved', M. Langer, M. Palonciová, G. Zoppellaro, S. V. Kershaw, A. L. Rogach, M. Otyepka, R. Zbořil, *ACS Nano* **2021**, *15*, 6582.
- [15] M. Li, T. Chen, J. J. Gooding, J. Liu, *ACS Sens.* **2019**, *4*, 1732.
- [16] W. Gao, H. Song, X. Wang, X. Liu, X. Pang, Y. Zhou, B. Gao, X. Peng, *ACS Appl. Mater. Interfaces* **2018**, *10*, 1147.
- [17] Y. Ma, A. Y. Chen, Y. Y. Huang, X. He, X. F. Xie, B. He, J. H. Yang, X. Y. Wang, *Carbon* **2020**, *162*, 234.
- [18] S. Zhu, Q. Meng, L. Wang, J. Zhang, Y. Song, H. Jin, K. Zhang, H. Sun, H. Wang, B. Yang, *Angew. Chem., Int. Ed.* **2013**, *52*, 3953.
- [19] D. Panáček, L. Zdražil, M. Langer, V. Šedajova, Z. Bađura, G. Zoppellaro, Q. Yang, E. P. Nguyen, R. Alvarez-Diduk, V. Hrubý, J. Kolařík, N. Chalmes, A. B. Bourlinos, R. Zbořil, A. Merkoci, A. Bakandritsos, M. Otyepka, *Small* **2022**, *18*, 2201003.
- [20] M. Zheng, S. Ruan, S. Liu, T. Sun, D. Qu, H. Zhao, Z. Xie, H. Gao, X. Jing, Z. Sun, *ACS Nano* **2015**, *9*, 11455.
- [21] X. Huang, F. Zhang, L. Zhu, K. Y. Choi, N. Guo, J. Guo, K. Tackett, P. Anilkumar, G. Liu, Q. Quan, H. S. Choi, G. Niu, Y.-P. Sun, S. Lee, X. Chen, *ACS Nano* **2013**, *7*, 5684.
- [22] S.-T. Yang, L. Cao, P. G. Luo, F. Lu, X. Wang, H. Wang, M. J. Meziani, Y. Liu, G. Q.-P. Sun, *J. Am. Chem. Soc.* **2009**, *131*, 11308.
- [23] D. Li, P. Jing, L. Sun, Y. An, X. Shan, X. Lu, D. Zhou, D. Han, D. Shen, Y. Zhai, S. Qu, R. Zbořil, A. L. Rogach, *Adv. Mater.* **2018**, *30*, 1705913.
- [24] L. Zdražil, S. Kalytchuk, K. Holá, M. Petr, O. Zmeškal, Š. Kment, A. L. Rogach, R. Zbořil, *Nanoscale* **2020**, *12*, 6664.
- [25] F. Yuan, Y.-K. Wang, G. Sharma, Y. Dong, X. Zheng, P. Li, A. Johnston, G. Bappi, J. Z. Fan, H. Kung, B. Chen, M. I. Saidaminov, K. Singh, O. Voznyy, O. M. Bakr, Z.-H. Lu, E. H. Sargent, *Nat. Photonics* **2019**, *14*, 171.
- [26] H. Choi, S.-J. Ko, Y. Choi, P. Joo, T. Kim, B. R. Lee, J.-W. Jung, H. J. Choi, M. Cha, J.-R. Jeong, I.-W. Hwang, M. H. Song, B.-S. Kim, J. Y. Kim, *Nat. Photonics* **2013**, *7*, 732.

- [27] S. Kalytchuk, L. Zdražil, M. Scheibe, R. Zbořil, *Nanoscale* **2020**, *12*, 8379.
- [28] S. Qu, X. Liu, X. Guo, M. Chu, L. Zhang, D. Shen, *Adv. Funct. Mater.* **2014**, *24*, 2689.
- [29] Y. Chen, M. Zheng, Y. Xiao, H. Dong, H. Zhang, J. Zhuang, H. Hu, B. Lei, Y. Liu, *Adv. Mater.* **2016**, *28*, 312.
- [30] B. Zhao, Z. Wang, Z. Tan, *Nat. Photonics* **2020**, *14*, 130.
- [31] G. A. M. Hutton, B. C. M. Martindale, E. Reisner, *Chem. Soc. Rev.* **2017**, *46*, 6111.
- [32] K. Holá, M. V. Pavliuk, B. Németh, P. Huang, L. Zdražil, H. Land, G. Berggren, H. Tian, *ACS Catal.* **2020**, *10*, 9943.
- [33] G. A. Hutton, B. Reuillard, B. C. Martindale, C. A. Caputo, C. W. Lockwood, J. N. Butt, E. Reisner, *J. Am. Chem. Soc.* **2016**, *138*, 16722.
- [34] K.-H. Ye, Z. Wang, J. Gu, S. Xiao, Y. Yuan, Y. Zhu, Y. Zhang, W. Mai, S. Yang, *Energy Environ. Sci.* **2017**, *10*, 772.
- [35] B. C. M. Martindale, G. A. M. Hutton, C. A. Caputo, E. Reisner, *J. Am. Chem. Soc.* **2015**, *137*, 6018.
- [36] S. Bhattacharyya, F. Ehrat, P. Urban, R. Teves, R. Wyrwich, M. Döblinger, J. Feldmann, A. S. Urban, J. K. Stolarczyk, *Nat. Commun.* **2017**, *8*, 1401.
- [37] T.-F. Yeh, C.-Y. Teng, S.-J. Chen, H. Teng, *Adv. Mater.* **2014**, *26*, 3297.
- [38] V. Strauss, J. T. Margraf, C. Dolle, B. Butz, T. J. Nacken, J. Walter, W. Bauer, W. Peukert, E. Spiecker, T. Clark, D. M. Guldi, *J. Am. Chem. Soc.* **2014**, *136*, 17308.
- [39] J. Schneider, C. J. Reckmeier, Y. Xiong, M. von Seckendorff, A. S. Susha, P. Kasák, A. L. Rogach, *J. Phys. Chem. C* **2017**, *121*, 2014.
- [40] Y. Xiong, J. Schneider, E. V. Ushakova, A. L. Rogach, *Nano Today* **2018**, *23*, 124.
- [41] F. Ehrat, S. Bhattacharyya, J. Schneider, A. Lof, R. Wyrwich, A. L. Rogach, J. K. Stolarczyk, A. S. Urban, J. Feldmann, *Nano Lett.* **2017**, *17*, 7710.
- [42] T. Zhang, J. Zhu, Y. Zhai, H. Wang, X. Bai, B. Dong, H. Wang, H. Song, *Nanoscale* **2017**, *9*, 13042.
- [43] M. Langer, M. Palonciová, M. Medved, M. Pykal, D. Nachtigallová, B. Shi, A. J. A. Aquino, H. Lischka, M. Otyepka, *Appl. Mater. Today* **2021**, *22*, 100924.
- [44] H. J. Yoo, B. E. Kwak, D. H. Kim, *Carbon* **2021**, *183*, 560.
- [45] G. Ragazzon, A. Cadranel, E. V. Ushakova, Y. Wang, D. M. Guldi, A. L. Rogach, N. A. Kotov, M. Prato, *Chem* **2021**, *7*, 606.
- [46] R. Kumari, S. K. Sahu, *Langmuir* **2020**, *36*, 5287.
- [47] L. Ai, Y. Yang, B. Wang, J. Chang, Z. Tang, B. Yang, S. Lu, *Sci. Bull.* **2021**, *66*, 839.
- [48] B. Wang, J. Yu, L. Sui, S. Zhu, Z. Tang, B. Yang, S. Lu, *Adv. Sci.* **2020**, *8*, 2001453.
- [49] H. Yu, R. Shi, Y. Zhao, G. I. N. Waterhouse, L.-Z. Wu, C.-H. Tung, T. Zhang, *Adv. Mater.* **2016**, *28*, 9454.
- [50] B. C. M. Martindale, G. A. M. Hutton, C. A. Caputo, S. Prantl, R. Godin, J. R. Durrant, E. Reisner, *Angew. Chem., Int. Ed.* **2017**, *56*, 6459.
- [51] B. Jana, Y. Reva, T. Scharl, V. Strauss, A. Cadranel, D. M. Guldi, *J. Am. Chem. Soc.* **2021**, *143*, 20122.
- [52] X. Xu, W. Tang, Y. Zhou, Z. Bao, Y. Su, J. Hu, H. Zeng, *Adv. Sci.* **2017**, *4*, 1700273.
- [53] Y. Yan, J. Chen, N. Li, J. Tian, K. Li, J. Jiang, J. Liu, Q. Tian, P. Chen, *ACS Nano* **2018**, *12*, 3523.
- [54] S. Zhu, Y. Song, X. Zhao, J. Shao, J. Zhang, B. Yang, *Nano Res.* **2015**, *8*, 355.
- [55] A. Cadranel, J. T. Margraf, V. Strauss, T. Clark, D. M. Guldi, *Acc. Chem. Res.* **2019**, *52*, 955.
- [56] A. Cadranel, P. Haines, R. Kaur, A. Menon, P. W. Münich, P. R. Schol, D. M. Guldi, *Adv. Energy Mater.* **2020**, *11*, 2002831.
- [57] L. F. D. L. e Freitas, B. Puértolas, J. Zhang, B. Wang, A. S. Hoffman, S. R. Bare, J. Pérez-Ramírez, J. W. Medlin, E. Nikolla, *ACS Catal.* **2020**, *10*, 5202.
- [58] J. Sun, Y. Yu, A. E. Curtze, X. Liang, Y. Wu, *Chem. Sci.* **2019**, *10*, 5519.
- [59] J. Xu, Z. Chen, H. Zhang, G. Lin, H. Lin, X. Wang, J. Long, *Sci. Bull.* **2017**, *62*, 610.
- [60] M. Kou, Y. Wang, Y. Xu, L. Ye, Y. Huang, B. Jia, H. Li, J. Ren, Y. Deng, J. Chen, Y. Zhou, K. Lei, L. Wang, W. Liu, H. Huang, T. Ma, *Angew. Chem., Int. Ed.* **2022**, *61*, e202200413.
- [61] M. Gu, D.-Y. Lee, J. Mun, D. Kim, H. Cho, B. Kim, W. Kim, G. Lee, B.-S. Kim, H. Kim, *Appl. Catal., B* **2022**, *312*, 121379.
- [62] G. Zoppellaro, A. Geies, V. Enkelmann, M. Baumgarten, *Eur. J. Org. Chem.* **2004**, *2004*, 2367.
- [63] G. Zoppellaro, A. Geies, K. K. Andersson, V. Enkelmann, M. Baumgarten, *Eur. J. Org. Chem.* **2008**, *2008*, 1431.
- [64] S. J. Zhu, Y. B. Song, J. Wang, H. Wan, Y. Zhang, Y. Ning, B. Yang, *Nano Today* **2017**, *13*, 10.
- [65] J. Liu, X. Liu, H. Luo, Y. Gao, *RSC Adv.* **2014**, *4*, 7648.
- [66] Y. Li, Y. Zhao, H. Nie, K. Wei, J. Cao, H. Huang, M. Shao, Y. Liu, Z. Kang, *J. Mater. Chem. A* **2021**, *9*, 515.
- [67] R. Ma, L. Wang, H. Wang, Z. Liu, M. Xing, L. Zhu, X. Meng, F.-S. Xiao, *Appl. Catal., B* **2019**, *244*, 594.
- [68] Q. Wu, J. Cao, X. Wang, Y. Liu, Y. Zhao, H. Wang, Y. Liu, H. Huang, F. Liao, M. Shao, Z. Kang, *Nat. Commun.* **2021**, *12*, 483.
- [69] Z. Wu, X. Li, Y. Zhao, Y. Li, K. Wei, H. Shi, T. Zhang, H. Huang, Y. Liu, Z. Kang, *ACS Appl. Mater. Interfaces* **2021**, *13*, 60561.
- [70] S. Stoll, A. Schweiger, *J. Magn. Reson.* **2006**, *178*, 42.
- [71] Y. Zhao, D. G. Truhlar, *Theor. Chem. Acc.* **2007**, *120*, 215.
- [72] R. Ditchfield, W. J. Hehre, J. A. Pople, *J. Chem. Phys.* **1971**, *54*, 724.
- [73] A. D. Laurent, D. Jacquemin, *Int. J. Quantum Chem.* **2013**, *113*, 2019.
- [74] J. D. Chai, M. Head-Gordon, *Phys. Chem. Chem. Phys.* **2008**, *10*, 6615.
- [75] F. Weigend, R. Ahlrichs, *Phys. Chem. Chem. Phys.* **2005**, *7*, 3297.
- [76] A. V. Marenich, C. J. Cramer, D. G. Truhlar, *J. Phys. Chem. B* **2009**, *113*, 6378.
- [77] C. A. Guido, A. Chrayteh, G. Scalmani, B. Mennucci, D. Jacquemin, *J. Chem. Theory Comput.* **2021**, *17*, 5155.
- [78] M. Frisch et al., *Gaussian 16, Revision B.01*, Gaussian Inc. Wallingford, CT **2016**.
- [79] J. Wang, R. M. Wolf, J. W. Caldwell, P. A. Kollman, D. A. Case, *J. Comput. Chem.* **2004**, *25*, 1157.
- [80] A. Cheng, W. A. Steele, *J. Chem. Phys.* **1990**, *92*, 3858.
- [81] P. J. Stephens, F. J. Devlin, C. F. Chabalowski, M. J. Frisch, *J. Phys. Chem.* **2002**, *98*, 11623.
- [82] A. D. Becke, *J. Chem. Phys.* **1993**, *98*, 5648.
- [83] J. Wang, P. Cieplak, P. A. Kollman, *J. Comput. Chem.* **2000**, *21*, 1049.
- [84] J. Wang, W. Wang, P. A. Kollman, D. A. Case, *J. Mol. Graph Model* **2006**, *25*, 247.
- [85] D. A. Case, T. A. Darden, T. E. Cheatham III, C. L. Simmerling, J. Wang, R. E. Duke, R. Luo, R. C. Walker, W. Zhang, K. M. Merz, B. Roberts, S. Hayik, A. Roitberg, G. Seabra, J. Swails, A. W. Götz, I. Kolossváry, K. F. Wong, F. Paesani, J. Vanicek, R. M. Wolf, J. Liu, X. Wu, S. R. Brozell, T. Steinbrecher, H. Gohlke, Q. Cai, X. Ye, J. Wang, M.-J. Hsieh, et al., *AMBER 12*, University of California, San Francisco **2012**.
- [86] W. L. Jorgensen, J. Chandrasekhar, J. D. Madura, R. W. Impey, M. L. Klein, *J. Chem. Phys.* **1983**, *79*, 926.
- [87] G. Bussi, D. Donadio, M. Parrinello, *J. Chem. Phys.* **2007**, *126*, 014101.
- [88] H. J. C. Berendsen, J. P. M. Postma, W. F. van Gunsteren, A. DiNola, J. R. Haak, *J. Chem. Phys.* **1984**, *81*, 3684.
- [89] B. Hess, H. Bekker, H. J. C. Berendsen, J. G. E. M. Fraaije, *J. Comput. Chem.* **1997**, *18*, 1463.
- [90] M. Parrinello, A. Rahman, *J. Appl. Phys.* **1981**, *52*, 7182.
- [91] T. Darden, D. York, L. Pedersen, *J. Chem. Phys.* **1993**, *98*, 10089.
- [92] D. Van Der Spoel, E. Lindahl, B. Hess, G. Groenhof, A. E. Mark, H. J. Berendsen, *J. Comput. Chem.* **2005**, *26*, 1701.
- [93] The PyMol Molecular Graphics System, Version 1.7.2.1, Schrodinger LLC **2014**.